Nanoscale Advances

ROYAL SOCIETY OF CHEMISTRY

PAPER

View Article Online
View Journal | View Issue

Cite this: *Nanoscale Adv.*, 2025, **7**, 4710

Petroleum coke-derived graphene as a low-cost electrode material for efficient perovskite solar cells†

Masfar Alkhatani, *[a] Mzoun M. Almutairi,[b] Mariam H. Alalwan,[b] Hawraa K. Algharash,[b] Raghad A. Aldossary,[b] Yahya A. Alzahrani,[a] Sultan Alenzi,[a] Ibtisam S. Almalki,[a] Ghazal S. Yafi,[c] Abdulmalik M. Alessa,[a] Faisal S. Alghannam,[a] Abdulaziz Aljuwayr,[a] Nouf K. Al-Saleem,*[b] Anwar Alanazi[a] and Masaud Almalki[a]

We present a cost-effective approach for converting petroleum coke into high-quality graphene *via* thermal desulfurization followed by electrochemical exfoliation. The synthesized graphene exhibited structural integrity and optoelectronic properties comparable to those of graphite-derived materials. Integrated as rear electrodes in perovskite solar cells (PSCs), the petcoke-derived graphene enabled devices to achieve a power conversion efficiency (PCE) of approximately 19.1%, with an open-circuit voltage (V_{oc}) exceeding 1.13 V and a fill factor (FF) of ~78%. The petcoke-derived graphene PSCs exhibited superior photovoltaic performance compared to those fabricated with commercial graphene, and demonstrated comparable efficiency to devices employing conventional gold electrodes. These findings highlight the potential of waste-derived graphene as a scalable, sustainable, and economically viable alternative to noble metal contacts, aligning with circular economy principles and advancing low-cost photovoltaic technologies.

Received 4th May 2025
Accepted 22nd June 2025

DOI: 10.1039/d5na00441a

rsc.li/nanoscale-advances

1 Introduction

Climate change and limited fossil fuels are pushing the world to switch to cleaner and more sustainable energy sources.[1–3] As nations commit to net-zero targets and decarbonization roadmaps, renewable energy technologies are playing a central role in reshaping energy infrastructure.[3–6] Among these, solar photovoltaics (PV) have emerged as a front-runner due to their scalability, minimal operational emissions, and capacity to directly convert abundant solar irradiation into electricity.[3,5] Crystalline silicon (c-Si), including monocrystalline (mono-Si) and multicrystalline (multi-Si) types, makes up about 95% of solar panels worldwide. Although mono-Si offers high efficiency (around 26.7%), producing c-Si cells involves energy-heavy steps like purification and crystallization, which raise environmental and cost concerns.[7–10] Gallium arsenide (GaAs) solar cells can reach over 30% efficiency, but their high cost limits their use in large-scale, land-based applications.[11] In contrast, second-generation thin-film solar cells, such as amorphous silicon (a-Si), cadmium telluride (CdTe), and copper indium gallium selenide (CIGS), offer potential benefits in terms of flexibility and lightweight integration. However, these systems have yet to replicate the market success of silicon due to concerns over long-term stability, toxicity of constituent elements, and supply chain constraints.[12,13]

To address these limitations, perovskite solar cells (PSCs) have emerged as one of the most transformative technologies in next-generation photovoltaics.[14–16] Since their first report in 2009 with a modest 3.8% PCE, PSCs have witnessed an unprecedented rise in performance, reaching certified efficiencies exceeding 26.7% as of 2025.[17] Their remarkable optoelectronic properties—including strong light absorption, long carrier diffusion lengths, tunable bandgaps, and solution-processability at low temperatures position PSCs as strong candidates for low-cost, high-efficiency, and flexible energy harvesting devices.[14–16,18]

Nonetheless, several challenges impede the commercial realization of PSCs. Key issues include stability under environmental stressors (*e.g.*, humidity, oxygen, light, and heat),[14,15] scalability of large-area fabrication, and high material costs, particularly those arising from noble metal electrodes such as gold (Au) and silver (Ag).[19] In this context, there is a growing interest in replacing conventional metal contacts with cost-effective, earth-abundant alternatives to improve both the economic and environmental profiles of PSCs.[20,21]

[a]*Future Energy Technologies Institute, King Abdulaziz City for Science and Technology (KACST), P.O. Box 6086, Riyadh 11442, Saudi Arabia. E-mail: mqhtani@kacst.gov.sa*

[b]*Department of Physics, College of Science and Humanities, Imam Abdulrahman Bin Faisal University, P.O. Box 1982, Jubail, Saudi Arabia. E-mail: nkalsaleem@iau.edu.sa*

[c]*Department of Chemistry, King Saud University, P.O. Box 2455, Riyadh, 11451, Saudi Arabia*

† Electronic supplementary information (ESI) available. See DOI: https://doi.org/10.1039/d5na00441a

Carbon-based materials, especially graphene, have attracted considerable attention as promising substitutes due to their outstanding electrical conductivity, chemical stability, mechanical flexibility, and optical transparency.[20–24] Graphene has been integrated into various parts of PSC architectures, including as transparent electrodes, hole/electron transport layers, and interfacial modifiers, with demonstrated improvements in both performance and device longevity.[20] Particularly, its use as a counter electrode has shown potential for cost reduction and enhanced moisture stability. However, most reported studies rely on graphene produced *via* chemical vapor deposition (CVD) or reduction of graphene oxide (GO) processes that are often expensive, multistep, and environmentally taxing, thereby limiting large-scale implementation.[20]

To address these limitations, researchers are actively exploring low-cost and sustainable feedstocks for graphene production. One compelling alternative is petroleum coke (petcoke), a carbon-rich byproduct of oil refining that is typically relegated to high-emission industrial uses such as metallurgical processes and fuel combustion.[25–27] Owing to its high fixed-carbon content, low volatile impurities, and global abundance, petcoke represents a largely underutilized waste stream with considerable potential for upcycling into high-value nanomaterials. Recent studies have demonstrated that electrochemical exfoliation of petcoke in aqueous electrolytes can yield conductive few-layer graphene through a simple, potentially scalable, and environmentally benign process, provided that the petcoke undergoes appropriate thermal pretreatment.[25–27] This post-thermal activation step plays a critical role in reducing impurities, enhancing graphitic ordering, and improving exfoliation efficiency.

In this study, we adapted the post-thermal activation step and reported an efficient approach to synthesize few-layer graphene with a much better yield from locally sourced petroleum coke using electrochemical exfoliation in sulfate-based electrolytes. The electrochemical technique itself promotes ion intercalation and subsequent exfoliation under mild conditions, offering a viable and sustainable pathway for large-scale graphene synthesis using a low-value carbon feedstock. The produced graphene was systematically characterized using structural, spectroscopic, and electronic techniques to assess its suitability as an electrode material. To evaluate its practical applicability, we integrated the petcoke-derived graphene as a rear electrode in planar perovskite solar cells, replacing conventional gold contacts. The photovoltaic performance of these devices was then systematically compared to reference devices fabricated with commercially available graphene and noble metal electrodes. Notably, the PSCs employing petcoke-derived graphene exhibited better performance compared to those using commercial graphene, and demonstrated comparable efficiency and stability to devices with traditional gold electrodes. These findings underscore the potential of petcoke upcycling as a cost-effective and scalable route for producing high-quality graphene for next-generation photovoltaic technologies.

2 Materials and methods

2.1 Materials

A local high sulfur content petroleum coke, ammonium sulfate, $(NH_4)_2SO_4$, high purity platinum electrode, fluorine-doped tin oxide (FTO) coated glass substrates, compact titanium dioxide (c-TiO_2), mesoporous titanium dioxide paste (TiO_2), formamidinium iodide (FAI), lead iodide (PbI_2), dimethylformamide (DMF), dimethyl sulfoxide (DMSO), and spiro-OMeTAD as the hole transport material. Dopants used with spiro-OMeTAD include lithium bis(trifluoromethanesulfonyl)imide (Li-TFSI), 4-*tert*-butylpyridine (*t*BP), and FK209 cobalt complex. Gold (Au) was used as the top electrode material. All materials were used as received from commercial suppliers.

2.2 Graphene production: electrochemical exfoliation

In the electrochemical exfoliation process, petroleum coke or pet coke will be compacted into the anode electrode in an electrochemical cell. The circuit will be completed by using a platinum electrode as a cathode. Both electrodes will be immersed in a cell bath. An appropriate electrolyte will be used inside the cell for the petroleum coke exfoliation. For example, ammonium sulfate, $(NH_4)_2SO_4$, an inorganic salt, will be used because of its high ionic mobility of its ions. To enhance the crystalline structure of the petroleum coke used in this study, a high-temperature pre-treatment was conducted at 1400 °C for 10 hours under an inert argon atmosphere. The exfoliation will be performed by applying a suitable voltage. We conducted preliminary optimization to determine the ideal exfoliation conditions, including voltage range, electrolyte concentration, and duration, to maximize graphene yield and minimize structural defects. After that, we applied a voltage range from 1–10 V for 8 hours until electrochemical exfoliation was completed. Finally, the graphene product was collected from the bath and separated using membrane filters. The obtained graphene underwent post-annealing at different temperatures for several hours in order to improve its conductivity.

2.3 Perovskite solar cell devices fabrication

Perovskite solar cells were fabricated on fluorine-doped tin oxide (FTO) glass substrates (1.7 cm × 2.6 cm), which were patterned by etching 0.5 cm of the conductive layer using zinc powder and 4 M HCl. Substrates underwent sequential ultrasonic cleaning in soap solution, distilled water, ethanol, and acetone, followed by UV-ozone treatment for enhanced surface activation.

A compact TiO_2 layer was deposited *via* spray pyrolysis from a precursor solution containing titanium diisopropoxide bis(acetylacetonate), acetylacetone, and ethanol. The substrates were maintained at 450 °C during and after deposition to ensure proper adhesion and crystallization. A mesoporous TiO_2 layer was subsequently applied using a commercial TiO_2 paste (Dyesol 18NR-T) *via* spin-coating at 4000 rpm for 30 seconds, followed by annealing at 450 °C for 30 minutes.

The perovskite active layer was prepared from a precursor solution comprising 1.6 M PbI_2, 1.51 M FAI, 0.04 M $PbBr_2$,

0.33 M MACl, and 0.04 M MABr dissolved in DMF : DMSO (8 : 1 v/v). The solution was deposited using a two-step spin-coating process (2000 rpm for 10 s, then 6000 rpm for 30 s), with chlorobenzene applied as an anti-solvent during the final 18 seconds. Films were annealed at 100 °C for 10 minutes and then at 150 °C for an additional 10 minutes. After that, the hole transport layer (HTL) was fabricated by spin-coating a solution of 102.72 mg spiro-OMeTAD in chlorobenzene, doped with Li-TFSI and 4-*tert*-butylpyridine (*t*BP), at 4000 rpm for 30 seconds.

2.4 Preparation of graphene electrode

Graphene electrodes were fabricated using the doctor blade coating technique. A homogeneous slurry was prepared by dispersing electrochemically exfoliated graphene in *N*-methyl-2-pyrrolidone (NMP) with 4 wt% polyvinylidene fluoride (PVDF) as a binder. The mixture was stirred overnight to ensure uniformity. The slurry was then applied onto a clean glass substrate using a doctor blade with a fixed blade height of approximately 100 μm. The coated films were dried at 80 °C for 1 hour to remove residual solvent. Once dried, the freestanding graphene film was carefully cut to the desired dimensions and transferred to the solar cell as the rear electrode, replacing the conventional gold contact. To improve adhesion and interfacial contact, the bottom surface of the freestanding graphene film (*i.e.*, the surface intended to face the hole transport layer) was pre-treated with mild oxygen plasma (10 W, 10 s) prior to transfer. This treatment increased the surface energy of the graphene, promoting stronger interfacial bonding without exposing the underlying organic layers to oxidative damage.

The transfer was conducted *via* a press-transfer method, in which the plasma-treated graphene film was manually aligned over the device surface and laminated using a soft polydimethylsiloxane (PDMS) stamp under gentle pressure (~2–5 N cm^{-2}) at room temperature for approximately 1 minute. After transfer, the assembled device was annealed at 80 °C for 10 minutes to further enhance bonding between the graphene electrode and the hole transport layer. While freestanding graphene electrodes are often associated with increased series resistance and reduced fill factor (FF) due to suboptimal interfacial contact, the combined surface activation and mechanical lamination techniques employed here mitigated these limitations. This approach ensured uniform contact, minimized interfacial voids or wrinkles, and enabled efficient charge extraction, contributing to the relatively high FF values obtained in our devices.

3 Results and discussion

Experimentally, locally sourced petroleum coke, pre-annealed at high temperatures for desulfurization, was successfully exfoliated into graphene-like structures using an electrochemical exfoliation (ECE) technique, as detailed in the Materials and methods section. This technique leverages the intercalation of electrolyte ions between the stacked graphitic layers of the carbonaceous precursor, promoting the delamination of these layers into few-layer or even monolayer graphene sheets,[27] as schematically illustrated in Fig. 1(a). In this procedure, the applied voltage drives the reduction of water at the cathode and the hydroxyl ions (OH^-) attack graphite at the edges and grain boundaries;[25–27] the oxidation at the edges and grain boundaries expands the graphite, facilitating the intercalation of sulfate ions (SO_4^{2-}); the reduction of SO_4^{2-} anions and oxidation of water generate various gases, such as SO_2, O_2, and others. The expanding gases separate the graphene layers, resulting in electrochemically exfoliated graphene (EEG). The efficiency of the ECE process and the quality of the resulting graphene are highly dependent on the intrinsic structural characteristics of the precursor material particularly its crystallinity, degree of graphitization, and lamellar ordering.[25,28]

To enhance the crystalline structure of the petroleum coke used in this study, a high-temperature pre-treatment was conducted at 1400 °C for 10 hours under an inert argon atmosphere. This specific thermal condition was selected based on its dual effect: it effectively facilitates the desulfurization of high-sulfur petroleum coke and simultaneously promotes graphitization by aligning aromatic carbon domains into ordered graphitic layers.[29,30] X-ray diffraction (XRD) analysis was performed on the coke samples before and after the thermal treatment. As shown in Fig. 1(b), the annealed sample exhibited a marked increase in the intensity and sharpness of the (002) diffraction peak, indicative of improved graphitic ordering. Quantitative analysis revealed that the degree of crystallinity increased to approximately 72%, confirming the transformation of the disordered carbon domains into a more ordered, graphite-like structure.[31] This enhancement in crystallinity significantly improves the material's suitability for electrochemical exfoliation and contributes to the production of high-quality graphene nanosheets.

Detailed morphological and compositional characterization of graphene-like structures obtained *via* electrochemical exfoliation of thermally treated petroleum coke were carried out using a transmitted electron microscope (TEM). Fig. 2(a) and (b) display low magnification images of transparent, ultrathin, and crumpled nanosheets morphological traits typically associated with few-layer graphene. Furthermore, high-resolution TEM in Fig. 2(c) unveils a well-defined, hexagonally arranged atomic lattice, characteristic of graphitic carbon. This lattice structure closely resembles that observed in electrochemically exfoliated graphene derived from natural graphite, suggesting that the exfoliation process preserves the intrinsic crystallinity of the precursor material. The selected area electron diffraction (SAED) pattern shown in the inset of Fig. 2(c) exhibits sharp, symmetric, and hexagonally arranged diffraction spots, unequivocally confirming the presence of a crystalline sp^2-bonded carbon framework.[27,29] The clarity and symmetry of the SAED pattern further attest to the high degree of structural order and the retention of graphitic domains after exfoliation. Collectively, these observations confirm the successful formation of few-layer graphene with preserved crystallinity from petroleum coke *via* electrochemical exfoliation.

Fig. 2(d) shows the corresponding energy-dispersive X-ray spectroscopy (EDX) spectrum, providing elemental insights into the composition of the exfoliated sheets. The dominant

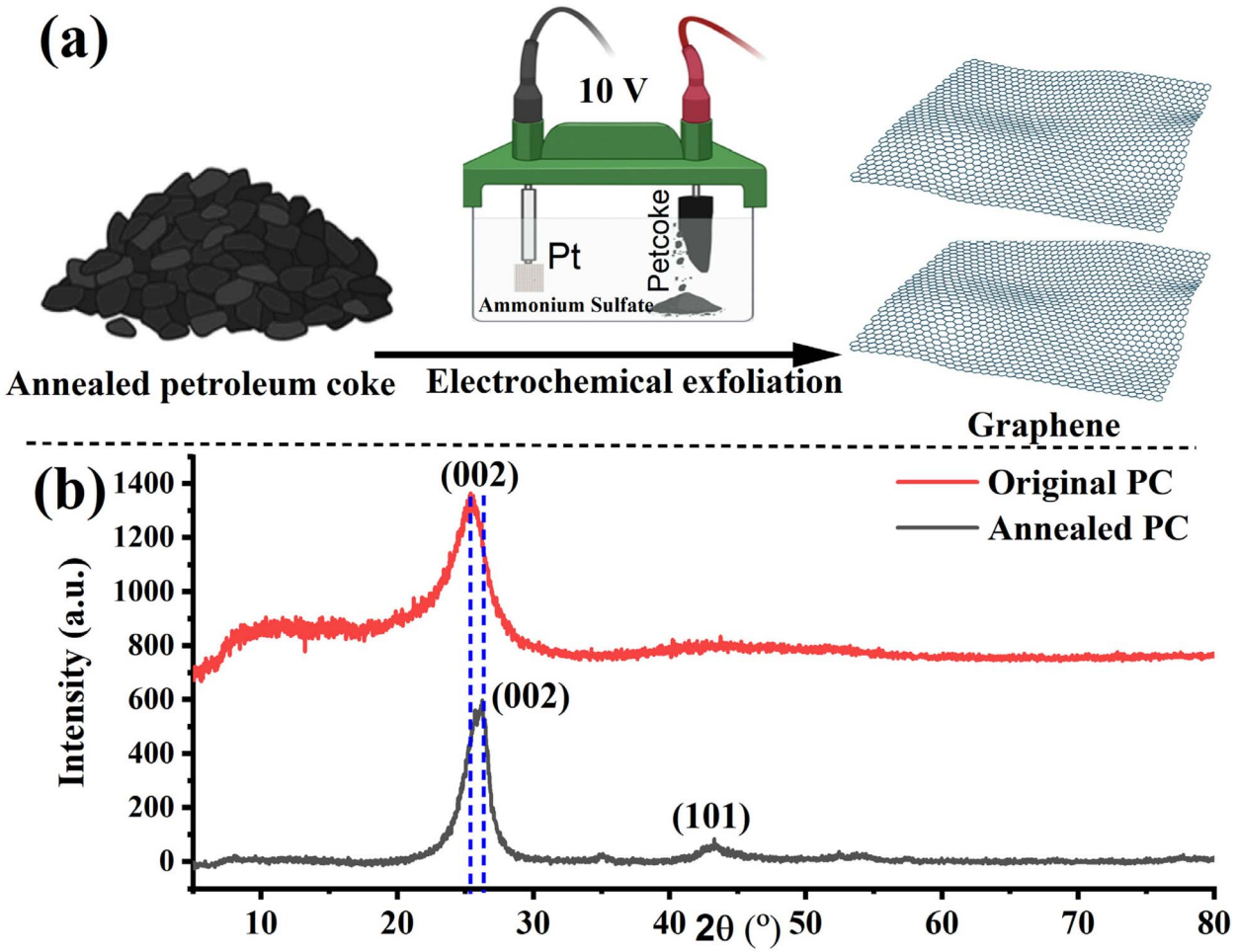

Fig. 1 (a) Schematic illustration of the electrochemical exfoliation (ECE) process, where electrolyte ions intercalate between the graphitic layers of thermally treated petroleum coke, leading to the formation of few-layer or monolayer graphene sheets. (b) X-ray diffraction (XRD) patterns of petroleum coke before and after thermal annealing at 1400 °C for 10 hours under inert atmosphere. The post-treatment pattern shows a significant sharpening and increase in the intensity of the (002) peak, indicating enhanced crystallinity. The calculated degree of crystallinity increased to ~72%, confirming the successful graphitization of the precursor material, thereby improving its suitability for high-yield graphene production *via* ECE.

peak at ~0.28 keV corresponds to carbon (C), affirming the carbon-rich nature of the product. A secondary peak appears at ~0.53 keV, corresponding to oxygen (O). This signal likely arises from surface oxygen-containing functional groups such as hydroxyl (–OH), carboxyl (–COOH), and carbonyl (C=O) moieties introduced during electrochemical exfoliation in aqueous or mildly oxidative conditions. These oxygen functionalities can also contribute to improved dispersibility and potential redox activity in energy storage applications. A weak yet distinguishable sulfur (S) peak at approximately 2.3 keV suggests the presence of residual sulfur species. While the intensity of this peak is low indicating that the high-temperature (1400 °C) thermal treatment was effective in removing a significant portion of sulfur the presence of trace sulfur implies incomplete desulfurization, which is common in high-sulfur petroleum coke precursors. Further optimization of the pretreatment conditions could potentially eliminate these residues. In addition to those peaks, strong copper (Cu) peaks near 8.0 keV and 9.0 keV are attributed to the copper TEM grid used during imaging. These peaks are instrumental artifacts and are not representative of the sample's intrinsic composition.

To further investigate the structural evolution during exfoliation, Raman spectroscopy was employed to analyze both the thermally treated petroleum coke and the resulting graphene,[28,32,33] as shown in Fig. 3. Raman spectroscopy is a powerful and widely used technique for characterizing carbon-based materials, particularly in distinguishing between graphitic domains, structural disorder, and the number of graphene layers. The characteristic Raman bands observed include the D band (~1350 cm^{-1}), associated with defect-induced breathing modes of sp^2 carbon rings; the G band (~1580 cm^{-1}), corresponding to the in-plane vibration (E_{2g} mode) of sp^2-hybridized carbon atoms; and the 2D band (~2700 cm^{-1}), which serves as a fingerprint for the number of graphene layers and the stacking order.[32] Raman spectra were collected using a 532 nm excitation laser on both samples drop-

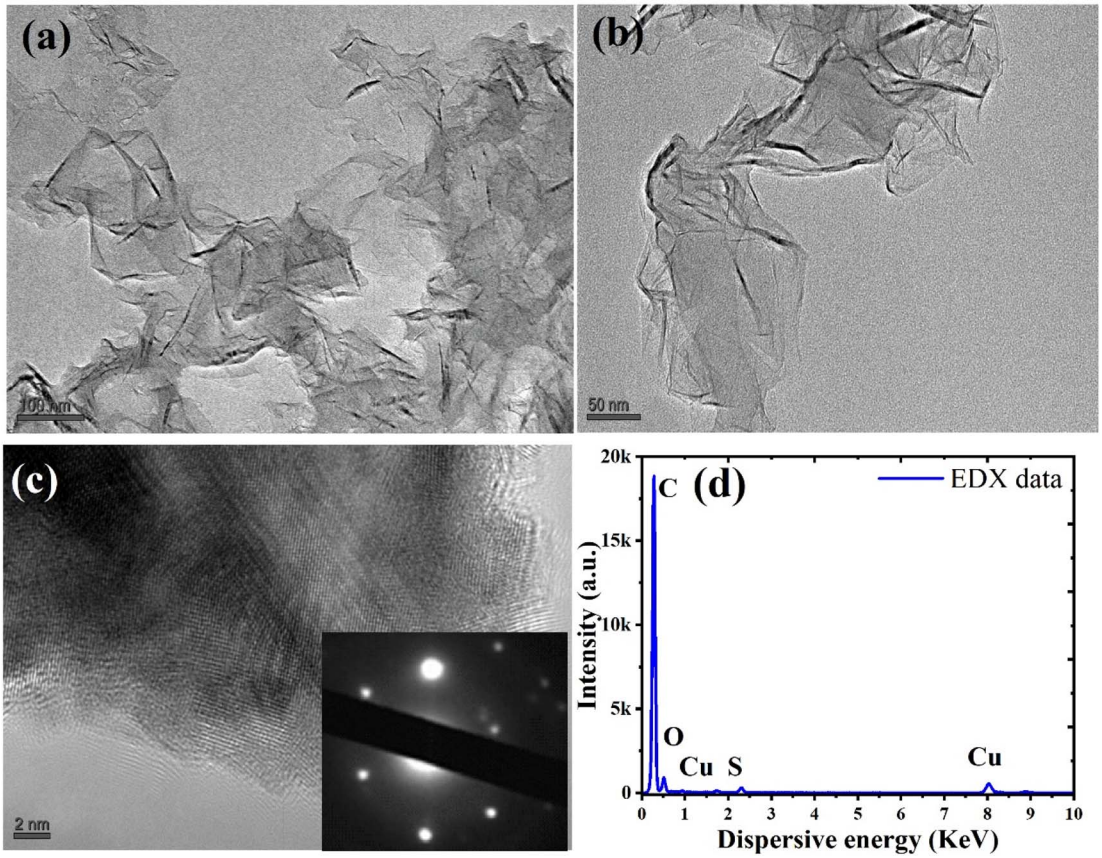

Fig. 2 TEM characterization and elemental analysis of graphene nanosheets obtained *via* electrochemical exfoliation of thermally treated petroleum coke. (a–c) Low and high-magnification TEM images showing few-layer, transparent, and wrinkled graphene sheets with lateral continuity and structural integrity. The inset in (c) displays a selected area electron diffraction (SAED) pattern, confirming the hexagonal crystalline structure of the graphene layers. (d) EDX spectrum collected from the exfoliated sample reveals dominant carbon content, with minor oxygen and sulfur signals. The copper signal originates from the TEM grid. The low sulfur intensity indicates efficient desulfurization during thermal treatment, supporting the purity and quality of the graphene product.

cast onto glass substrates. The spectrum of the annealed petroleum coke (red curve) displays a prominent D band, a broadened G band, and a weak, broad 2D band. This indicates the presence of partially graphitized domains with a significant degree of disorder, likely due to defects, edge states, and residual functional groups such as hydroxyl and epoxide moieties.

In contrast, the Raman spectrum of the exfoliated graphene (black curve) reveals a significantly sharper and more intense 2D band centered at ~2700 cm^{-1}, indicative of few-layer graphene. The I_{2D}/I_G intensity ratio ranges from 0.5 to 0.7, suggesting the presence of two to five graphene layers with relatively low stacking disorder. Furthermore, the I_D/I_G ratio, which varies between 0.8 and 0.9 across different regions of the sample, reflects the presence of some residual defects, yet within a range acceptable for conductive applications.[32,33] These findings confirm the successful exfoliation of graphene sheets from petroleum coke and the partial restoration of sp^2 graphitic domains. To evaluate the scalability and batch-to-batch reproducibility of our electrochemically exfoliated graphene, we developed a standardized protocol with tight control over key parameters, including electrolyte composition, applied voltage, exfoliation duration, and post-annealing conditions. These parameters were optimized to ensure consistency across production runs. To confirm reproducibility, three independent exfoliation batches were performed under identical conditions. The resulting graphene films demonstrated consistent electrical performance, with sheet resistance values varying by less than ±7%, as determined using a four-point probe method. Morphological analyses using TEM revealed a uniform flake thickness distribution, with the majority of flakes exhibiting 4–6 layers.

Prior to integrating coke-derived graphene into perovskite solar cell architectures, it was essential to evaluate its electrical properties to ensure its suitability as a conductive electrode material. To this end, freestanding films were fabricated *via* vacuum filtration from dispersions of the exfoliated graphene sheets. The baseline electrical conductivity of the thermally treated but non-exfoliated petroleum coke was measured at 65 S m^{-1}, reflecting limited structural order and high defect density. Following electrochemical exfoliation, a notable enhancement in conductivity was observed, with the coke-derived graphene films reaching a conductivity of 125 S m^{-1}, more than doubling the initial value. This improvement is attributed to the

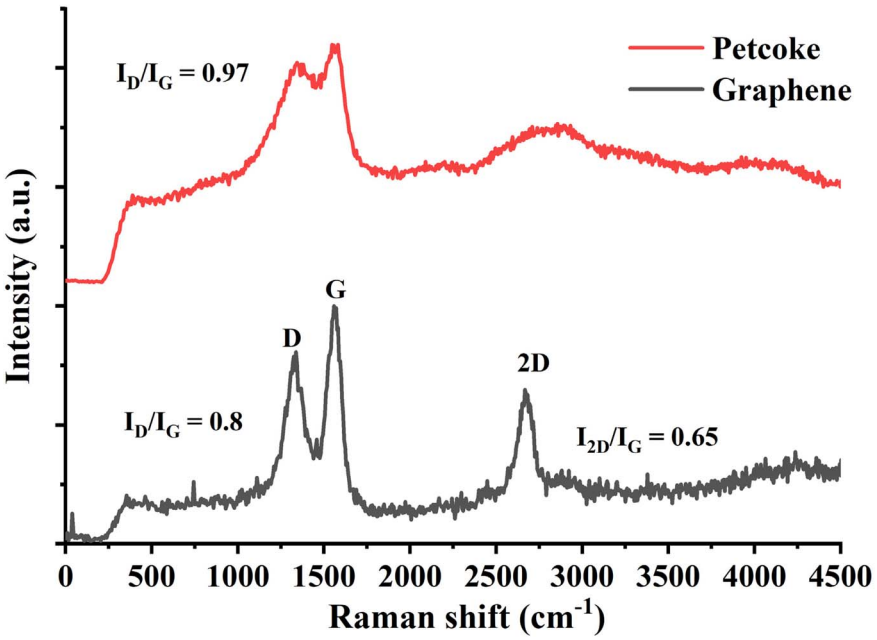

Fig. 3 Raman spectra of thermally treated petroleum coke (red curve) and electrochemically exfoliated graphene (black curve), recorded using a 532 nm excitation laser. The spectrum of the annealed coke shows a prominent D band (~1350 cm^{-1}), a broad G band (~1580 cm^{-1}), and a weak, broad 2D band (~2700 cm^{-1}), indicating partial graphitization with significant structural disorder. In contrast, the exfoliated graphene exhibits a sharper 2D peak and reduced D-band intensity, consistent with the formation of few-layer graphene. The intensity ratios I_D/I_G (0.8–0.9) and I_{2D}/I_G (0.5–0.7) confirm improved structural ordering and the presence of thin graphene sheets with moderate defect density.

increased restoration of sp^2 carbon domains and the partial removal of insulating oxygenated functional groups during the exfoliation process. To further optimize the electrical performance, post-synthesis thermal annealing was employed at elevated temperatures. The exfoliated films were annealed under inert atmosphere at 500 °C and 1100 °C for 12 hours. After annealing at 500 °C, the conductivity increased to 225 S m^{-1}, and further rose to 310 S m^{-1} upon annealing at 1100 °C. The achieved value is in the range of conductivity needed for Li ion batteries.[34,35] This progressive enhancement is primarily attributed to the thermal removal of residual oxygen-containing functional groups (*e.g.*, hydroxyl, carboxyl, and epoxide) as shown in the FTIR spectra illustrated in Fig. 1S,† as well as adsorbed impurities that act as scattering centers. The additional increase observed beyond 500 °C may result from molecular rearrangement and further graphitization, leading to improved π-conjugation and reduced defect density in the carbon lattice.[27,36]

Next, we fabricated two PSC devices with and without coke derived graphene electrode and their photovoltaics was performed and compared. The general and common structure of PSCs, as illustrated in Fig. 4(a), consists of multiple functional layers: a cathode at the top, typically made of conductive materials like gold or silver, which collects electrons; a hole transport layer (HTL) that facilitates the movement of positive charge carriers (holes) towards the cathode; an absorber layer made of perovskite material, such as methylammonium lead iodide ($CH_3NH_3PbI_3$), which is responsible for light absorption and generating electron–hole pairs; an electron transport layer (ETL) that transports electrons to the anode; and a glass substrate coated with a transparent conductive oxide like ITO or FTO, serving as the anode.[37] The working principle involves sunlight absorption by the perovskite layer, generating excitons that separate into free electrons and holes. Electrons are transported through the ETL to the anode while holes move through the HTL to the cathode, creating an electric current.[38,39]

To evaluate the structural and optical properties of the synthesized perovskite layer prior to full device fabrication, the perovskite films were deposited on fluorine-doped tin oxide (FTO) substrates sequentially coated with compact TiO_2 (c-TiO_2) and mesoporous TiO_2 (m-TiO_2). The detailed fabrication process is outlined in the Materials and methods section. Structural and morphological analyses were carried out using scanning electron microscopy (SEM), X-ray diffraction (XRD), UV-Vis absorption spectroscopy, and photoluminescence (PL) measurements, as presented in Fig. 4. The SEM images, shown in Fig. 4(b), reveal a densely packed perovskite film with well-defined grains and significantly enhanced grain size. Larger grains are known to reduce grain boundary density, thereby minimizing non-radiative recombination pathways and enhancing charge carrier transport factors that directly contribute to improved photovoltaic performance.[24,38]

XRD analysis, presented in Fig. 4(c), provides insights into the crystallographic structure of the perovskite layer. The diffraction peaks observed at 13.90°, 19.73°, 24.16°, 27.85°, 31.17°, 34.31°, 39.86°, and 42.29° correspond to the (001), (011), (111), (002), (012), (112), (022), and (122) crystal planes of the α-phase formamidinium lead iodide (α-$FAPbI_3$), respectively.[24] Notably, the prominent diffraction peak at 13.90°, corresponding to the (001) orientation, is present in both control and PEAI-

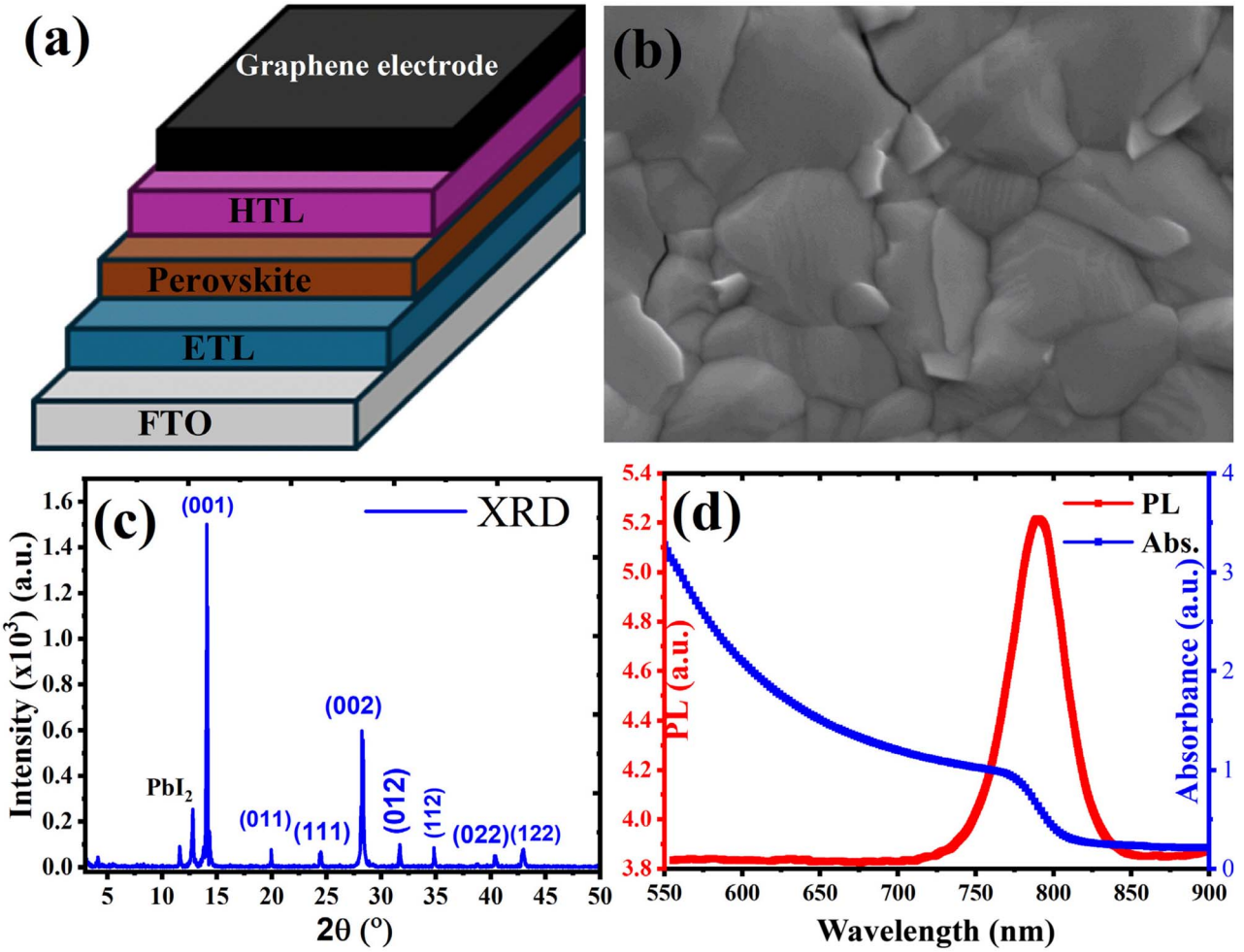

Fig. 4 Structural and optical characterization of the fabricated perovskite films. (a) Schematic of the layered substrate structure: FTO/c-TiO_2/m-TiO_2/perovskite. (b) SEM image showing the surface morphology of the perovskite film, revealing enlarged and well-connected grains, indicative of improved crystallinity and reduced grain boundary defects. (c) X-ray diffraction (XRD) pattern of the perovskite film, displaying sharp diffraction peaks at 13.90°, 19.73°, 24.16°, 27.85°, 31.17°, 34.31°, 39.86°, and 42.29°, corresponding to the (001), (011), (111), (002), (012), (112), (022), and (122) lattice planes of the α-$FAPbI_3$ phase, confirming high crystallinity and phase purity. (d) Optical properties of the perovskite film as measured by UV-Vis absorption and photoluminescence (PL) spectroscopy. The absorption edge at ~815 nm corresponds to a band gap of ~1.55 eV, while the strong PL emission peak at the same wavelength indicates low trap-state density and high radiative recombination efficiency.

modified perovskite films, indicating the dominant presence of the photoactive black phase. Optical characterization of the film was conducted using UV-Vis absorption spectroscopy, as shown in Fig. 4(d). The absorption spectrum exhibits a sharp absorption edge at approximately 815 nm, which corresponds to an optical band gap of 1.55 eV, consistent with values reported for high-quality α-$FAPbI_3$ perovskite films. Complementary photoluminescence (PL) spectroscopy also revealed a strong and distinct emission peak, closely aligned with the absorption edge, further confirming the formation of a phase-pure perovskite structure with minimal trap-assisted recombination.

To investigate the feasibility of petroleum coke-derived graphene as a cost-effective alternative to noble metal electrodes, perovskite solar cells (PSCs) were fabricated using graphene as the rear electrode and benchmarked against control devices employing thermally evaporated gold. Both types of devices shared an identical n–i–p configuration: FTO/c-TiO_2/m-TiO_2/perovskite/PEAI/spiro-OMeTAD/electrode. Photovoltaic characterization revealed that perovskite solar cells (PSCs) employing petcoke-derived, electrochemically exfoliated graphene as the rear electrode exhibited a power conversion efficiency (PCE) of approximately 19.1%. The devices achieved an open-circuit voltage (V_{oc}) exceeding 1.12 V, a fill factor (FF) approaching 75%, and a short-circuit current density (J_{sc}) of ~23.1 mA cm^{-2}, as shown in Fig. 5(a) and (b) and summarize in Table 1. These performance metrics suggest efficient charge extraction and low interfacial recombination losses at the graphene–perovskite interface. The enhancement in V_{oc} is attributed to favorable energy level alignment, where literature-reported work function values for electrochemically exfoliated graphene (typically ~4.6–4.9 eV)[40,41] are positioned between the valence band maximum of $MAPbI_3$ (~5.4 eV) and the HOMO level of spiro-OMeTAD (~5.1 eV). This alignment is expected to promote effective hole extraction and minimize interfacial energy barriers.

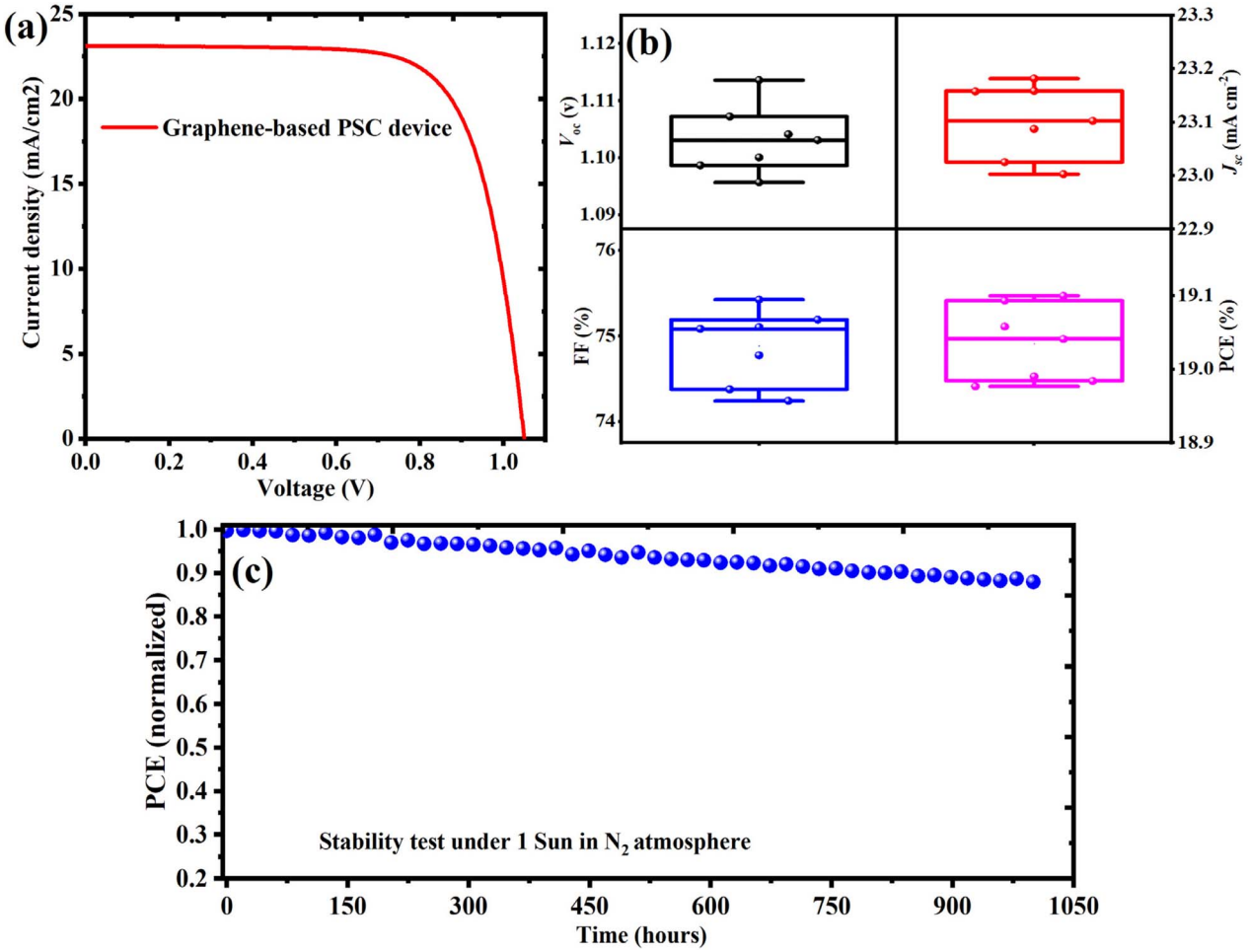

Fig. 5 (a) Current density–voltage (J–V) curve of the best-performing perovskite solar cell (PSC) incorporating an exfoliated graphene rear electrode, showing a PCE of 19.1%. (b) Statistical distribution of photovoltaic parameters (V_{oc}, J_{sc}, FF, and PCE) measured across five independent devices, demonstrating good reproducibility. (c) Long-term operational stability of the unencapsulated graphene-based PSCs under continuous 1 sun illumination in a nitrogen (N_2) atmosphere, retaining over 90% of the initial PCE after 900 hours.

Consequently, the use of graphene contributes to the observed improvements in both V_{oc} and FF, which are typically associated with suppressed interfacial recombination and enhanced carrier transport. Although direct characterization techniques such as time-resolved photoluminescence (TRPL) and electrochemical impedance spectroscopy (EIS) are routinely used to probe carrier dynamics and quantify non-radiative losses, these measurements were not conducted in the present study due to instrumental constraints. Nevertheless, the elevated V_{oc} and the absence of pronounced hysteresis in the current–voltage (J–V) curves provide indirect evidence of reduced non-radiative recombination at the graphene–perovskite interface. Future work will incorporate TRPL and EIS analyses to enable a more comprehensive understanding of the interfacial charge dynamics and to further validate the role of petcoke-derived graphene in defect passivation and charge transfer enhancement.

We evaluated the long-term operational stability of the fabricated PSC device employing exfoliated graphene electrodes. The devices were subjected to continuous illumination under 1 sun equivalent intensity using an LED solar simulator in an inert nitrogen (N_2) atmosphere. As shown in Fig. 5(c), the

Table 1 Comparison of the photovoltaics performance of petcoke-derived graphene-based PSCs with analogous devices employing commercial graphene and gold (Au) electrodes

PSC device structure	J_{sc} (mA cm^{-2})	V_{oc} (V)	FF (%)	PCE (%)
FTO/TiO_2/perovskite/spiro-OMeTAD/petcoke-derived graphene	23.1	1.12	75	19.1
FTO/TiO_2/perovskite/spiro-OMeTAD/commercial graphene	22.5	1.1	73	18
FTO/TiO_2/perovskite/spiro-OMeTAD/Au	25.3	1.13	76	22

normalized power conversion efficiency (PCE) remained above 90% of the initial value for over 900 hours, demonstrating excellent operational durability. These results highlight the intrinsic stability of the graphene-based PSCs under prolonged operating conditions.

To contextualize this performance, we compared petcoke-derived graphene-based PSC device to similar PSC architectures using commercial graphene and gold (Au) electrodes. As summarized in Table 1, the Au-based device delivered the highest PCE of 22.0%, attributed to its higher $J_{sc} \sim 25.3$ mA cm^{-2}, while V_{oc} and FF remained similar (~1.13 V and 76%) see Fig. 2S.† The device employing commercial graphene exhibited a lower PCE of 18.0%, confirming that our exfoliated, petcoke-derived graphene offers superior performance among carbon-based alternatives. Notably, while the Au-based control device exhibits the highest PCE and J_{sc}, our graphene-based PSC stands out by maintaining high V_{oc} and FF while replacing a costly, diffusion-prone noble metal with a sustainable, low-cost carbon electrode. The slightly lower J_{sc} in graphene-based devices may stem from differences in electrical conductivity or interfacial contact quality. Further optimization, such as doping, conductivity enhancement, or improved interfacial engineering may help close this performance gap. This comparison underscores the strong potential of exfoliated graphene derived from petroleum coke as a scalable and environmentally sustainable electrode material for next-generation perovskite solar cells.

To assess the performance of our fabricated perovskite solar cell (PSC) employing petcoke-derived exfoliated graphene as the rear electrode, we benchmarked its photovoltaic characteristics against previously reported graphene-based PSCs[21–24] that incorporate graphene or graphene-derivative rear contacts. Table 2 summarizes key photovoltaic parameters, including short-circuit current density (J_{sc}), open-circuit voltage (V_{oc}), fill factor (FF), and power conversion efficiency (PCE), for representative device architectures.

As seen in the Table 2, our device demonstrates a high open-circuit voltage of 1.12 V and a fill factor of 75%, contributing to a competitive PCE of 19.1%. This performance surpasses many of the previously reported graphene-based PSCs, particularly those using untreated graphene or graphene oxide, which typically suffer from lower FF and V_{oc} due to interfacial energy mismatches or poor film conductivity. While some devices employing optimized SnO_2 scaffolds exhibit slightly higher FF, the V_{oc} achieved in our work is among the highest reported for graphene-based electrodes, underscoring the favorable energy alignment between the petcoke-derived graphene and the hole transport layer. The enhanced device performance can be attributed to both the improved conductivity of the thermally annealed graphene and the effective interface formed between the exfoliated graphene and the perovskite/spiro-OMeTAD layers. This comparative analysis highlights the viability of petroleum coke as a low-cost and scalable precursor for high-performance graphene electrodes in PSCs, providing an eco-friendly alternative to conventional gold contacts without compromising efficiency.

4 Conclusions

In conclusion, this work demonstrates a viable and sustainable strategy for converting locally sourced petroleum coke into high-quality, few-layer graphene through a thermally assisted electrochemical exfoliation (ECE) method. The optimized high-temperature desulfurization significantly enhanced the graphitization degree of the coke precursor, facilitating efficient exfoliation and yielding graphene with high crystallinity and low defect density, as confirmed by TEM, SAED, and Raman analyses. Post-exfoliation annealing further improved the electrical conductivity of the graphene films, achieving values up to 310 S m^{-1}. Petroleum coke-derived graphene, implemented as rear electrodes in perovskite solar cells, enabled a power conversion efficiency of ≈19% and delivered an enhanced open-circuit voltage compared to conventional gold contacts. In a direct comparison with devices employing commercial graphene and gold electrodes, the petcoke-graphene cells outperformed their commercial-graphene counterparts and demonstrated comparable efficiency and operational stability to gold-based devices. These results reflect the favorable electronic alignment at the graphene–perovskite interface, which suppresses non-radiative recombination, and establish petroleum coke as a low-cost, scalable feedstock for producing conductive graphene offering a viable route to eco-friendly, metal-free solar technologies that advance circular-economy and cost-reduction objectives.

Data availability

The data supporting this article have been included as part of the ESI.†

Table 2 Benchmarking the photovoltaic performance of the fabricated petcoke-derived graphene-based PSC against previously reported perovskite solar cells (PSCs) incorporating graphene or graphene-derived rear electrodes. Metrics include short-circuit current density (J_{sc}), open-circuit voltage (V_{oc}), fill factor (FF), and power conversion efficiency (PCE)

PSC device structure	J_{sc} (mA cm^{-2})	V_{oc} (V)	FF (%)	PCE (%)	Ref.
Glass/FTO/TiO_2/perovskite/spiro-OMeTAD/graphene	19.17	0.96	67.22	12.37	21
Graphene-based flexible perovskite solar cells	21	0.99	72	15	22
FTO/SnO_2/perovskite/spiro-OMeTAD/graphene layer	22.69	1.05	77	18.25	23
FTO/TiO_2/perovskite/spiro-OMeTAD/graphene oxide	25.06	0.984	69	17	24
FTO/TiO_2/perovskite/spiro-OMeTAD/petcoke-derived graphene	23.1	1.12	75	19.1	This work

Author contributions

M. A. (Masfar Alkhatani) and N. K. A.-S. (Nouf K. Al-Saleem) conceived and supervised the project. M. A. designed the experiments, interpreted the results, and wrote the initial draft of the manuscript. M. M. A., M. H. A., H. K. A., and R. A. A. conducted material synthesis, characterization, and performance measurements. Y. A. A., S. A., I. S. A., and G. S. Y. contributed to device fabrication and optimization. A. M. A., F. S. A., and A. A. participated in data analysis, figure preparation, and literature review. A. A. (Anwar Alanazi) and M. A. (Masaud Almalki) provided critical insights into experimental methodology and manuscript revision. All authors reviewed the manuscript and approved the final version.

Conflicts of interest

There are no conflicts to declare.

Acknowledgements

This work was funded by King Adulaziz City for Science and Technology (KACST), Saudi Arabia.

References

1 A. J. Al-Yasiri, *Akkad J. Contemp. Econ. Stud.*, 2022, **1**, 186–196.
2 R. B. Jackson, P. Friedlingstein, C. Le Quéré, S. Abernethy, R. M. Andrew, J. G. Canadell, P. Ciais, S. J. Davis, Z. Deng, Z. Liu, J. I. Korsbakken and G. P. Peters, *Environ. Res. Lett.*, 2022, **17**, 031001.
3 A. Hu, S. Levis, G. A. Meehl, W. Han, W. M. Washington, K. W. Oleson, B. J. van Ruijven, M. He and W. G. Strand, *Nat. Clim. Change*, 2016, **6**, 290–294.
4 M. V. Dambhare, B. Butey and S. V. Moharil, *J. Phys.: Conf. Ser.*, 2021, **1913**, 012053.
5 N. Kannan and D. Vakeesan, *Renewable Sustainable Energy Rev.*, 2016, **62**, 1092–1105.
6 F. J. M. M. Nijsse, J.-F. Mercure, N. Ameli, F. Larosa, S. Kothari, J. Rickman, P. Vercoulen and H. Pollitt, *Nat. Commun.*, 2023, **14**, 6542.
7 C. Ballif, F.-J. Haug, M. Boccard, P. J. Verlinden and G. Hahn, *Nat. Rev. Mater.*, 2022, **7**, 597–616.
8 A. Müller, M. Ghosh, R. Sonnenschein and P. Woditsch, *Mater. Sci. Eng., B*, 2006, **134**, 257–262.
9 C. C. Farrell, A. I. Osman, R. Doherty, M. Saad, X. Zhang, A. Murphy, J. Harrison, A. S. M. Vennard, V. Kumaravel, A. H. Al-Muhtaseb and D. W. Rooney, *Renewable Sustainable Energy Rev.*, 2020, **128**, 109911.
10 E. A. Alsema and M. J. de Wild, *MRS Online Proc. Libr.*, 2006, **895**, 305.
11 T. Ibn-Mohammed, S. C. L. Koh, I. M. Reaney, A. Acquaye, G. Schileo, K. B. Mustapha and R. Greenough, *Renewable Sustainable Energy Rev.*, 2017, **80**, 1321–1344.
12 W. A. Badawy, *J. Adv. Res.*, 2015, **6**, 123–132.
13 A. Shah, P. Torres, R. Tscharner, N. Wyrsch and H. Keppner, *Science*, 1999, **285**, 692–698.
14 M. Noman, Z. Khan and S. T. Jan, *RSC Adv.*, 2024, **14**, 5085–5131.
15 C. Yang, W. Hu, J. Liu, C. Han, Q. Gao, A. Mei, Y. Zhou, F. Guo and H. Han, *Light: Sci. Appl.*, 2024, **13**, 227.
16 G. Szabó, N.-G. Park, F. De Angelis and P. V. Kamat, *ACS Energy Lett.*, 2023, **8**, 3829–3831.
17 Y. Huang, K. Yan, X. Wang, B. Li, B. Niu, M. Yan, Z. Shen, K. Zhou, Y. Fang, X. Yu, H. Chen, L. Zhang and C.-Z. Li, *Adv. Mater.*, 2024, **36**, 2408101.
18 D. Jayan Koodali, *Phys. Status Solidi A*, 2024, **221**, 2300782.
19 T. Seyisi, B. G. Fouda-Mbanga, J. I. Mnyango, Y. B. Nthwane, B. Nyoni, S. Mhlanga, S. P. Hlangothi and Z. Tywabi-Ngeva, *Energy Rep.*, 2025, **13**, 1400–1415.
20 K. Gong, J. Hu, N. Cui, Y. Xue, L. Li, G. Long and S. Lin, *Mater. Des.*, 2021, **211**, 110170.
21 P. You, Z. Liu, Q. Tai, S. Liu and F. Yan, *Adv. Mater.*, 2015, **27**, 3632–3638.
22 J. Yoon, H. Sung, G. Lee, W. Cho, N. Ahn, H. S. Jung and M. Choi, *Energy Environ. Sci.*, 2017, **10**, 337–345.
23 C. Zhang, S. Wang, H. Zhang, Y. Feng, W. Tian, Y. Yan, J. Bian, Y. Wang, S. Jin, S. M. Zakeeruddin, M. Grätzel and Y. Shi, *Energy Environ. Sci.*, 2019, **12**, 3585–3594.
24 E. A. Alghamdi, I. S. Almalki, R. Sai, M. H. Alkahtani, G. S. Yafi, Y. A. Alzahrani, S. M. Alenzi, A. Aljuwayr, A. Aldukhail, K. E. Alzahrani, F. S. Alfaifi, H. S. Althobaiti, W. K. Alenazi, A. Q. Alanazi and M. Almalki, *Mater. Today Sustain.*, 2024, **28**, 101022.
25 T. C. Achee, W. Sun, J. T. Hope, S. G. Quitzau, C. B. Sweeney, S. A. Shah, T. Habib and M. J. Green, *Sci. Rep.*, 2018, **8**, 14525.
26 J. T. Hope, W. Sun, S. Kewalramani, S. Saha, P. Lakhe, S. A. Shah, M. J. Mason, M. J. Green and R. A. Hule, *ACS Appl. Nano Mater.*, 2020, **3**, 10303–10309.
27 S. Saha, P. Lakhe, M. J. Mason, B. J. Coleman, K. Arole, X. Zhao, S. Yakovlev, S. Uppili, M. J. Green and R. A. Hule, *npj 2D Mater. Appl.*, 2021, **5**, 75.
28 A. C. Ferrari, J. C. Meyer, V. Scardaci, C. Casiraghi, M. Lazzeri, F. Mauri, S. Piscanec, D. Jiang, K. S. Novoselov, S. Roth and A. K. Geim, *Phys. Rev. Lett.*, 2006, **97**, 187401.
29 C. Kumar, A. Gupta, P. Saharan, M. Singh and S. R. Dhakate, *Diamond Relat. Mater.*, 2023, **140**, 110433.
30 H. Al-Haj-Ibrahim and B. I. Morsi, *Ind. Eng. Chem. Res.*, 1992, **31**, 1835–1840.
31 X. Xu, D. Cao, Y. Wei, A. Wang, G. Chen, T. Wang, G. Wang and X. Chen, *ACS Omega*, 2024, **9**, 2443–2456.
32 A. C. Ferrari and D. M. Basko, *Nat. Nanotechnol.*, 2013, **8**, 235–246.
33 J.-B. Wu, M.-L. Lin, X. Cong, H.-N. Liu and P.-H. Tan, *Chem. Soc. Rev.*, 2018, **47**, 1822–1873.
34 M. Park, X. Zhang, M. Chung, G. B. Less and A. M. Sastry, *J. Power Sources*, 2010, **195**, 7904–7929.
35 M. Ashuri, Q. He and L. L. Shaw, *Nanoscale*, 2016, **8**, 74–103.
36 R. E. Franklin and J. T. Randall, *Proc. R. Soc. London, Ser. A*, 1951, **209**, 196–218.
37 Q. Chen, N. De Marco, Y. Yang, T.-B. Song, C.-C. Chen, H. Zhao, Z. Hong, H. Zhou and Y. Yang, *Nano Today*, 2015, **10**, 355–396.

38 M. M. Osman, A. Q. Alanazi, T. I. Alanazi, M. H. Alkahtani, A. M. El-naggar, A. A. Albassam, A. M. Aldhafiri, M. Al-Gawati, M. Almalki, S. M. Alenzi and M. D. Mensi, *Sol. Energy Mater. Sol. Cells*, 2024, **273**, 112955.
39 M. Alkahtani, A. A. Almuqhim, H. Qasem, N. Alsofyani, A. Alfahd, S. M. Alenzi, A. Aljuwayr, Y. A. Alzahrani, A. Al-Badri, M. H. Alotaibi, A. Bagabas, A. N. AlHazaa and P. R. Hemmer, *Nanomaterials*, 2021, **11**, 2909.
40 Y.-J. Yu, Y. Zhao, S. Ryu, L. E. Brus, K. S. Kim and P. Kim, *Nano Lett.*, 2009, **9**, 3430–3434.
41 J. Torop, V. Palmre, M. Arulepp, T. Sugino, K. Asaka and A. Aabloo, *Carbon*, 2011, **49**, 3113–3119.